Ocean Dynamics (2022) 72:679–693
https://doi.org/10.1007/s10236-022-01525-9

Mesoscale eddy variability in the Caribbean Sea

Margarita E. López-Álzate[1,2] · Juan-Manuel Sayol[3] · Ismael Hernández-Carrasco[4] · Andrés F. Osorio[1,2] · Evan Mason[5] · Alejandro Orfila[5]

Received: 9 March 2022 / Accepted: 25 August 2022 / Published online: 6 September 2022

Abstract
The spatial distribution, and the monthly and seasonal variability of mesoscale eddy observations derived from the AVISO eddy atlas are assessed in the Caribbean Sea during 1993–2019. The average lifetime for the whole set of eddies is 62 ± 37 days, mean amplitude of 7 ± 4 cm for cyclonic and 7 ± 4 cm for anticyclonic and mean radius of 100 ± 31 km for cyclonic and 108 ± 32 km for anticyclonic. Cyclonic eddies are on average more nonlinear than anticyclonic ones. The spatio-temporal variability in the number of eddy observations is evaluated against the Mean Eddy Kinetic Energy (MEKE) derived from geostrophic currents as well as from seasonal winds. Spatial distribution of eddy observations is correlated with MEKE while the migration of the intertropical convergence zone explains the advection of eddies towards the southern part of the basin.

Keywords Mesoscale eddies · Caribbean Sea · Seasonal variability · Self-organizing map (SOM) · Eddy observations

1 Introduction

Mesoscale eddies are ocean structures in nearly geostrophic balance of paramount importance in the redistribution of water properties across ocean basins (Capet et al. 2008; Farneti et al. 2010; Gaube et al. 2015). These vortexes have diameters that vary between 5 and 200 km and lifetimes spanning from weeks to months (Chelton et al. 2011).

Mesoscale eddies typically form from initial instabilities created by the interaction between strong horizontally sheared currents or from current-topography interactions in boundary currents (Bracco et al. 2008; Rennie et al. 2007; Soutelino et al. 2013), although other mechanisms may exist (e.g., Ji et al. 2018). Depending on which side with respect to the main flow they form, eddies may contain either relatively warm or cold water compared to their surroundings. Accordingly, eddies will rotate anticyclonically or cyclonically in the Northern Hemisphere. Warm-core eddies display a central Sea Surface Height (SSH) of a few to tens of centimeters higher than outer water, while cold-core eddies present a central SSH lower than its surroundings. Although warm-core eddies can trap and transport a wide variety of nutrients and aquatic life (Karstensen et al. 2017), cold-core eddies tend to carry a greater amount of biological activity with them (Chang et al. 2018). Sometimes, mesoscale eddies may also take the form of well defined current rings that

Responsible Editor: Sheila Natalí Estrada Allis

✉ Alejandro Orfila
alejandro.orfila@csic.es

Margarita E. López-Álzate
melopeza@unal.edu.co

Juan-Manuel Sayol
juanma.sayol@ua.es

Ismael Hernández-Carrasco
ihernandez@socib.es

Andrés F. Osorio
afosorioar@unal.edu.co

Evan Mason
evanmason@gmail.com

[1] Oceánicos, Facultad de Minas, Universidad Nacional de Colombia, Medellín, Colombia

[2] CEMarin, Carrera 21 # 35-53, Barrio La Soledad, Bogotá, Colombia

[3] Department of Applied Mathematics, University of Alicante, San Vicente del Raspeig 03690, Alicante, Spain

[4] Balearic Islands Coastal Observing and Forecasting System (SOCIB), Palma 07122, Mallorca, Spain

[5] Mediterranean Institute for Advanced Studies, IMEDEA (CSIC-UIB), Esporles 07190, Mallorca, Spain

extend to large depths (Fratantoni and Richardson 2006; de Jong et al. 2016).

Previous experimental and numerical studies have suggested that mesoscale variability in the Caribbean Sea is dominated by warm-core anticyclonic eddies. Regarding their mechanisms of formation, some authors have associated the formation of Caribbean Sea eddies with flow-topography interaction (Jouanno et al. 2008, 2009; van der Boog et al. 2019; Molinari et al. 1981; Goni and Johns 2003; Jochumsen et al. 2010), the meandering of the Caribbean boundary current (Andrade and Barton 2000), and the growth of baroclinic instabilities around river plume fronts (Chérubin and Richardson 2007). Indeed some eddies form from cold filaments at the eastern side of the basin thus leading to a cooling of the Caribbean Sea interior, while at the same time they transport salinity anomalies from Amazon and Orinoco river plumes westward (van der Boog et al. 2019).

In the Caribbean, eddies are transported westward by the mean flow after their formation, thus entirely affecting the ecosystem around them as they transport larvae and nutrients offshore (Andrade and Barton 2005; Baums et al. 2006). During their propagation, eddies become more energetic and increase their amplitude (Carton and Chao 1999; van der Boog et al. 2019). Although this intensification is evident from observations, only a few studies have elaborated the dynamics of this strengthening (Carton and Chao 1999; Pauluhn and Chao 1999; Andrade and Barton 2000; Richardson 2005). Based on surface drifters, Richardson (2005) suggested that the anticyclonic shear of the Caribbean Current could amplify anticyclonic eddies. Besides, Andrade and Barton (2000) found, based on satellite altimetry, a direct relationship between the maximum curl of the wind stress and the westward intensification of anticyclones. Jouanno et al. (2009) used a regional model to study the life cycle of Caribbean anticyclones and computed the mechanical energy balance of the flow in this region. Although this balance shows that baroclinic instabilities provide the necessary energy for the westward growth of anticyclones, it does not explain what drives the westward intensification of anticyclones. More recently, van der Boog et al. (2019) have mainly attributed this westward intensification of anticyclonic eddies to the role of salinity gradients generated by upwelling events and river outflow combined with the westward rise of the background velocity shear, which altogether strengthen the thermal wind balance within the vortex.

In this work we analyze the spatial and temporal variability of observed mesoscale eddies from 1993 to 2019 (both included). Caribbean eddies are known to have pronounced variability in both space and time with large impact in transporting and redistributing water mass properties across the basin. Several studies have been carried out to describe how these eddies form, propagate and dissipate in the Caribbean region by ship-drift, buoys, drifters, satellites observations and numerical models. These eddies may potentially be playing an important role in the North Atlantic circulation by exchanging Caribbean Current mass and momentum with the surrounding waters. Despite the importance of these structures neither a dedicated systematic census of observed eddies focused on the Caribbean Sea nor an analysis of their seasonal variability from a statistical standpoint have been performed yet, beyond some global studies (e.g., Chelton et al. 2011; Mason et al. 2014; Conti et al. 2016). We address this gap by providing a detailed statistical description of eddy properties, as well as of the main environmental drivers that may affect their seasonal variability.

2 The Caribbean basin

The Caribbean is a semi-enclosed sea that covers the area between 8°N–25°N and 85°W–55°W (Fig. 1a). It is confined on the south and west by the South and Central American continents, and on the north and the east by the Greater Antilles and the chain of Lesser Antilles Islands Arc (Andrade 2000; Johns et al. 2002; Richardson 2005; Jury 2011). The Caribbean Sea is connected by many passages to the tropical Atlantic Ocean through the Lesser Antilles (Fig. 1a). The bottom topography of the Caribbean Sea can be divided into five basins: between the Lesser Antilles Arc and Las Aves Ridge lies the Granada Basin, the Venezuelan Basin in the east, and the Colombian Basin in the west. These basins are separated by the Beata Ridge which crosses the central Caribbean. The Central American Rise separates the Cayman and Colombian Basins and the Cayman Ridge which divides the Cayman and Yucatan Basins. The Caribbean Sea is connected with the Gulf of Mexico at the north through the Yucatan Strait.

The most important sources of water in the Caribbean Sea are provided by the returning deep southwestward Gulf Stream waters in the northern and northeastern edges, and by the North Brazil Current (NBC) on the southeastern edge. Atlantic waters contribute in three different ways: the North Equatorial Current passing through the Leeward Islands of the Lesser Antilles with an estimated inflow of ~8 Sv, the flow in the windward Passage between Cuba and Hispaniola with ~7 Sv, and the flow through the Mona Passage between Hispaniola and Puerto Rico with ~ 3 Sv. The NBC transports fresh water from the Orinoco River, flowing northwestward into the Caribbean basin through the "Windward Island" with ~6 Sv and Saint Vincent and Saint Lucia with ~4 Sv forming a boundary current known as the Caribbean Current (CC) (Richardson 2005; Jury 2011) (Fig. 1c). The CC extends towards the Panama Isthmus where a branch continues towards the Yucatan basin, while another branch may recirculate to form the

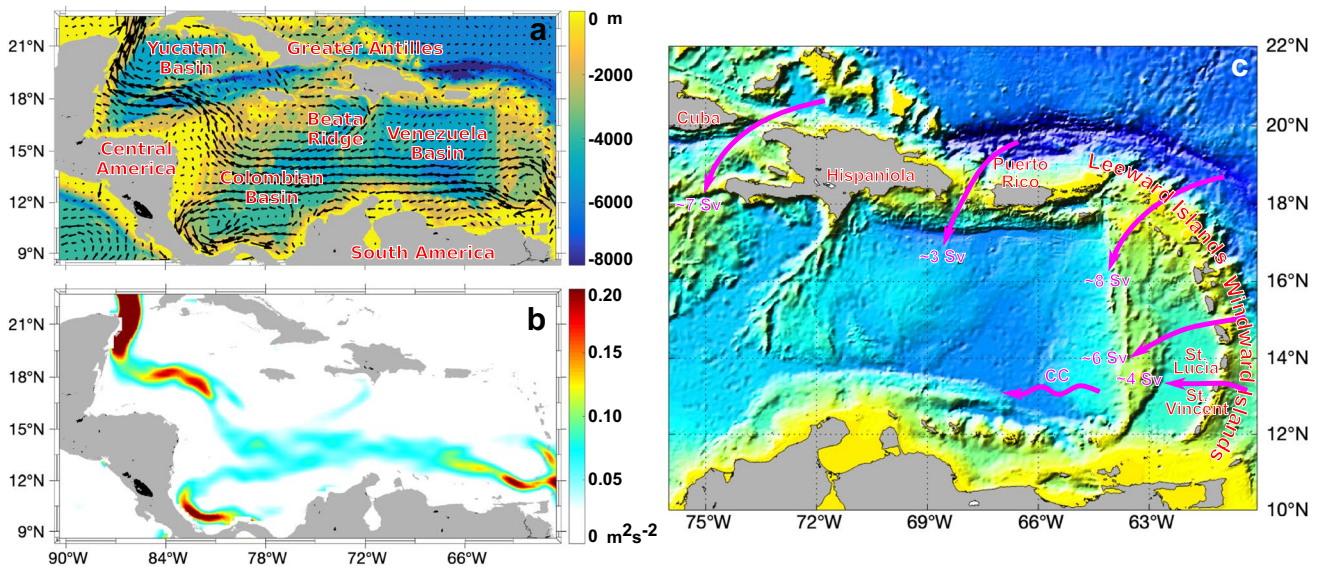

Fig. 1 (**a**) Geographic location of the Caribbean Sea with the different basins and bathymetry contour (in m). Arrows correspond to the mean geostrophic currents for the period 1993–2019 derived from AVISO SLA. This data is available since 1993 at Copernicus Climate Change Service (https://climate.copernicus.eu/), with spatial resolution of 0.25°×0.25° (only each 9 arrows have been plotted for simplicity). (**b**) MKE ($u_g^2 + v_g^2$) obtained from geostrophic velocities for the period 1993–2019 (units in m^2/s^2). (**c**) Schematic view of the main inflow sources in the Caribbean basin

Panama-Colombia Gyre, from which under favorable wind conditions a counter current can form and reach La Guajira peninsula, known as the Caribbean Counter Current (CCC) (Orfila et al. 2021).

A strong Ekman component of the transport is generated in the Caribbean Sea by the Trade Winds (see Fig. 11 in Appendix A), which blow from the northeast-east-southeast depending, to a large extent, on the latitudinal position of the Intertropical Convergence Zone (ITCZ) and of the North Atlantic subtropical high (Schneider et al. 2014; Orejarena-Rondón et al. 2022).

3 Eddy trajectory atlas

Detected eddies for the period between 1993 and 2019 are obtained from the eddy trajectory atlas in its delayed-time version 2.0exp. This product provides information on mesoscale eddies derived from Sea Level Anomalies (SLA) and it is produced by SSALTO/DUACS and distributed by AVISO+ with support from CNES, Oregon State University and NASA (AVISO 2020). The originally weekly SLA were interpolated by SSALTO/DUACS to have daily fields. Then the atlas was constructed over those daily SLA maps, thus including daily information on properties of each detected eddy such as radius, amplitude, rotational speed, polarity as well as the time when it was observed, the coordinates of the estimated center, the track identification or the observation number. The algorithms used in this product are derived from the methodology developed by Schlax and Chelton (2016), where an eddy is considered to be a propagating, compact, coherent structure in the space-time SSH field. Among the processes followed by the algorithm are included the filtering of sea level anomalies, the eddy identification, the characterization of main properties of eddies (size, amplitude, rotational speed) and the eddy tracking. Throughout next sections and for the sake of clarity we will refer by eddy observation every single daily data of a given track, while by an eddy we will refer to the statistical average of all available observations for the same track. For further details on the eddy detection algorithm the reader is referred to Appendix B.

The number of detected eddies during 1993–2019 in the Caribbean basin (red box in Fig. 2) is 2246 (only 110 detected outside, between 5 and 15° N) almost equally distributed between cyclonic eddies (CE) (54%) and anticyclonic eddies (AE) (46%). The initial positions (yellow dots) and trajectories are displayed in Fig. 2 for CE (a) and for AE (b). As seen, most eddies have their origin in the eastern Caribbean Sea and in the northwestern side. In the former case, eddies are advected by the CC whose origin is the North Equatorial Current passing through the Lesser Antilles and deflected at 76°W towards the south of Panama following the CCC. Both the CC and the CCC are clearly recognizable from the Mean Kinetic Energy (MKE=$u_g^2 + v_g^2$) of the geostrophic currents, $\mathbf{v}_g$ (see Fig. 1b).

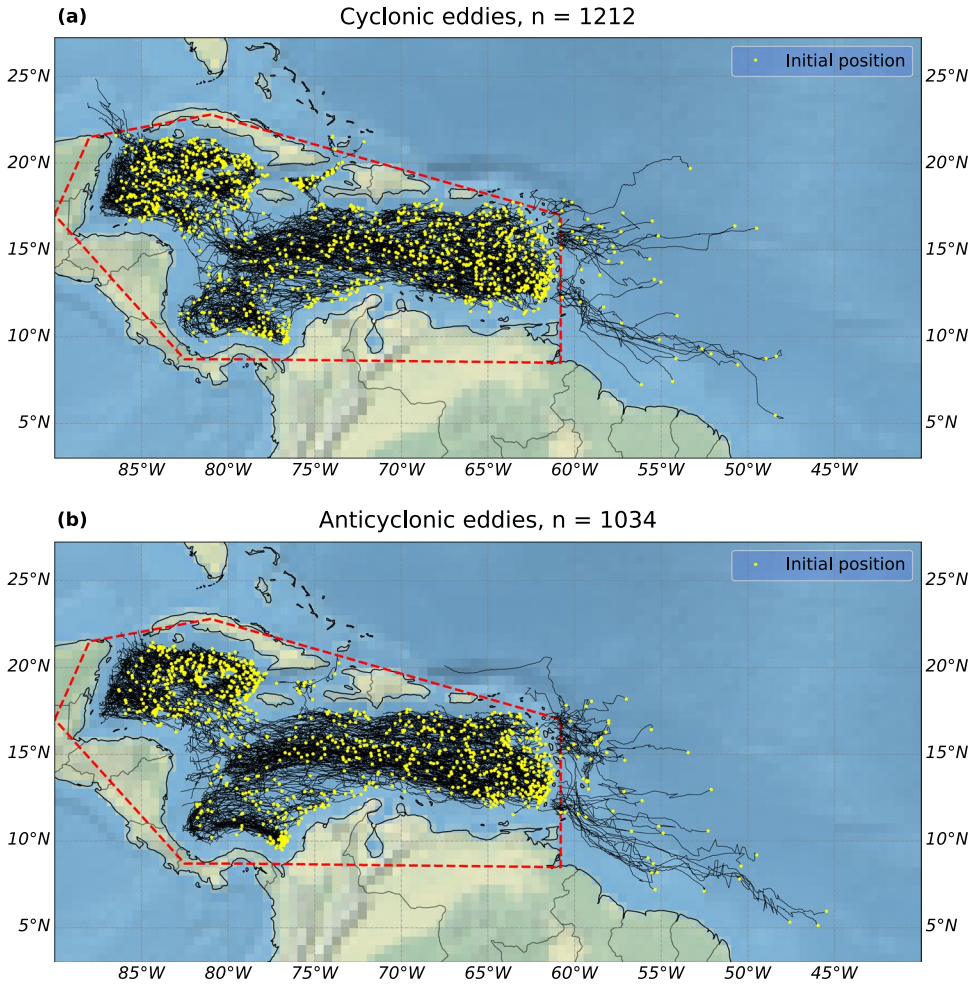

Fig. 2 Trajectories of eddies for the period 1993–2019 from the AVISO atlas: (**a**) for cyclonic eddies (CE) and (**b**) for anticyclonic eddies (AE). The dashed red line delimits the area of study and yellow dots indicate initial location of eddies

4 Results

4.1 Statistical description of Caribbean Sea eddy properties

Mean and standard deviation of observed eddies in the Caribbean Sea are shown in Fig. 3 for relevant parameters: lifetime (a–c), amplitude (d–f), radius (g–i) and nonlinearity (j–l).

The average lifetime for the whole set of eddies is 62 ± 37 days (mean ± standard deviation), and 60 ± 35 days for CE and 64 ± 40 days for AE with the longest-lived lasting 319 days and 290 days for CE and AE, respectively (Fig. 3a–c). A vast majority of mesoscale eddies (> 85%) have a lifetime shorter than 120 days.

The eddy amplitude, defined as the largest sea level difference between the eddy core and the sea level height average at its edge perimeter is shown in Fig. 3d–f. Mean amplitude is 7 ± 4 cm for CE (Fig. 3e) and 7 ± 4 cm for AE (Fig. 3f). These results agree with those of Gaube (2013), who found that the eddy field in the Caribbean Sea is characterized by average eddy amplitudes of 7.1 cm. However, Chelton et al. (2011) pointed out that the predominance of small eddy amplitudes may raise concerns that their distribution is influenced by the procedure applied to detect eddies, which may sometimes be biased low by 1 or 2 cm in regions of very energetic mesoscale variability and by less than 1 cm in less energetic regions due to the complex geometry of many eddies.

There are no significant differences between both eddy polarities in the effective radius scale. Radii range from 50 to 250 km, as expected from the spatial resolution of the altimetry. The mean radius is 100 ± 31 km for CE and 108 ± 32 km for AE (Fig. 3h, i). This result is consistent with the latitudinal distribution of eddy sizes described by Chelton et al. (2011), where eddies of around 100 km of radius are found in the near-equatorial regions to later monotonically decrease up to 80 km at 20° of latitude. We note that these length-scales of eddies and eddy-like features are constrained by the Rossby radius of deformation (Chelton et al. 1998).

The eddy nonlinearity is defined as, $\varepsilon = U/c$ with U being the rotational speed and c the celerity of the advection on the geostrophic flow, also called translational speed. A value

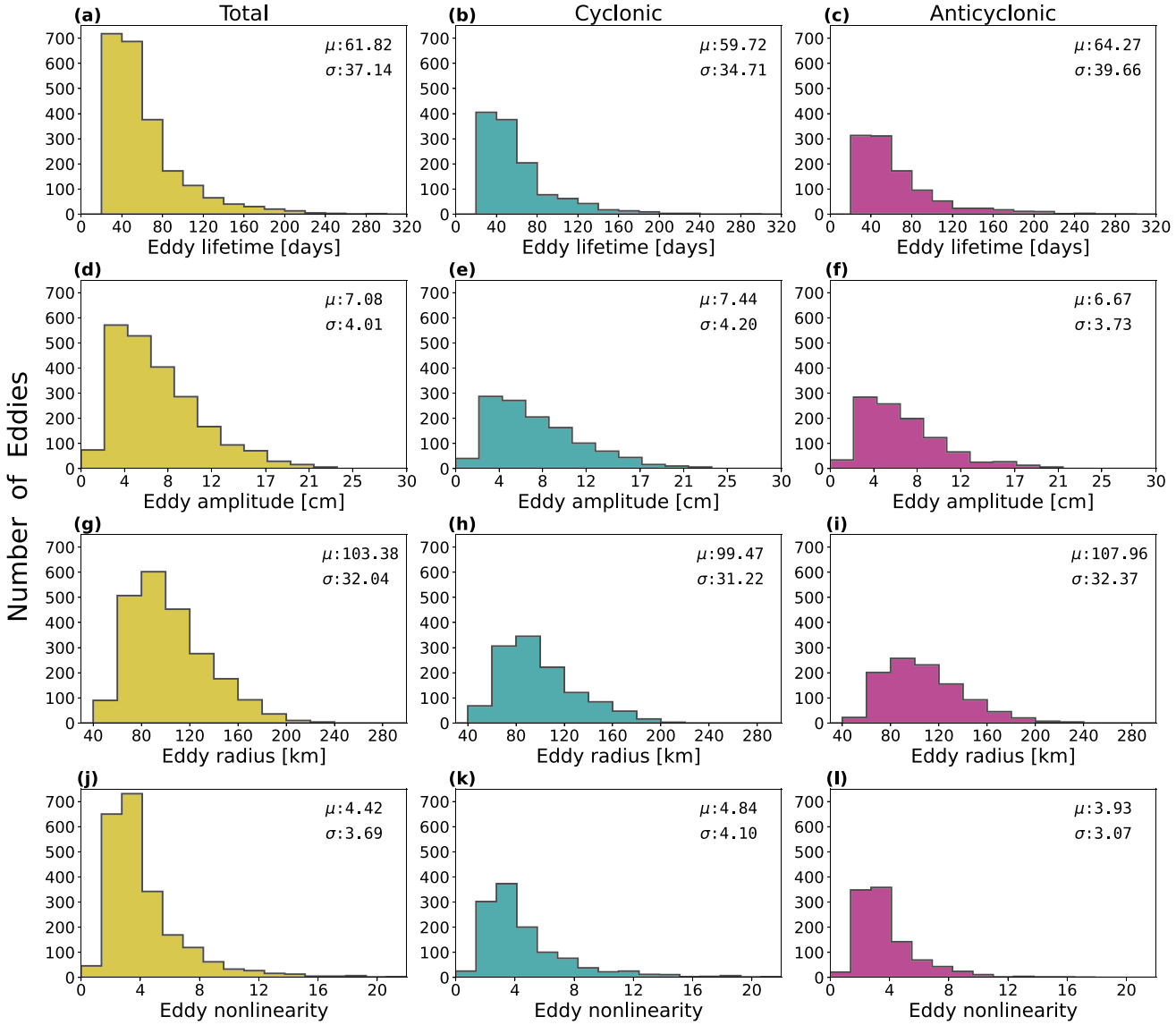

Fig. 3 Histogram of properties for the total number of eddies (left), for CE (center) and for AE (right). First row correspond to eddy lifetime (in days), second to amplitude (in cm), third radius (in km), and fourth nonlinearity (dimensionless)

of $\varepsilon \geq 1$ implies that the mesoscale eddy cannot be regarded as a linear wave disturbance propagating through a nearly stationary medium, but instead is capable of modifying the medium by advecting a trapped fluid parcel as it translates transporting water properties such as heat and salt, as well as other biogeochemical characteristics such as nutrients and phytoplankton (Chelton et al. 2011). Figure 3j–l show that, all combined, CE and ACE are nonlinear on average, with over 90% of eddies showing $\varepsilon \geq 1$. Indeed, over 25% of eddies are highly nonlinear with $\varepsilon > 5$, being CE more nonlinear than ACE on average (5 ± 4 against 4 ± 3). These values of ε are in good agreement with the results that can be inferred from Chelton et al. (2011) in the Caribbean Sea region.

To examine the general patterns in the eddy properties we have proceeded to normalize the amplitude, radii and nonlinearity of eddies according to their lifetime. To this end, for each eddy the first value of lifetime is considered its birth (normalized lifetime of 0), and the last value its death (normalized lifetime of 1). Subsequently, the lifetime of each eddy has been divided in regular sub periods of 0.02. Later, the mean value of each parameter within each sub period has been computed and scaled with respect to the value at birth, which provides a normalized value of 1 for each eddy and for all properties at the initial time. Finally, all eddy observations within the corresponding sub period have been averaged. As a result, a general mean curve showing the evolution of each eddy property

for all eddy observations and for a normalized lifetime is obtained.

Results for the amplitude, radii and nonlinearity for the whole set of eddies, CE and AE are displayed in Fig. 4. As seen, when all eddies are considered, they tend to increase substantially in amplitude and radius during the first part of their life (around 150% in amplitude and 35% in radius) reaching the maximum development at around 0.6 of their normalized lifetime (Fig. 4a). The same trend is obtained for the CE and AE subset of data (Fig. 4b and c, respectively). Once eddies have reached their maximum amplitude they tend to spend another 20% of their lifetime with the same amplitude, to later start a fast decay till reaching a value close to 50% larger of their initial amplitude at the end of their lifetime. A similar process occurs with the radii, with small differences between AE and CE. At the end of their life, the radius tends to be about 10% larger than in the beginning. An interesting point is that the peak in the amplitude is clearer defined for CE than for ACE, since the latter shows a plateau for about 20% of normalized eddy lifetime. Hence, this result could be potentially used to predict eddy lifetime of CE, partially disagreeing with the statement of Chelton et al. (2011), who argued that the amplitude of an eddy is not enough to determine its longevity. Regarding nonlinearity, it strongly increases (about 200%) on average during the first third of eddy lifetime, then it keeps rather stable although with some marked oscillations, which suggests large differences between eddies. At the end of their observed life, eddies are about 2.5–3 times more nonlinear than in the beginning.

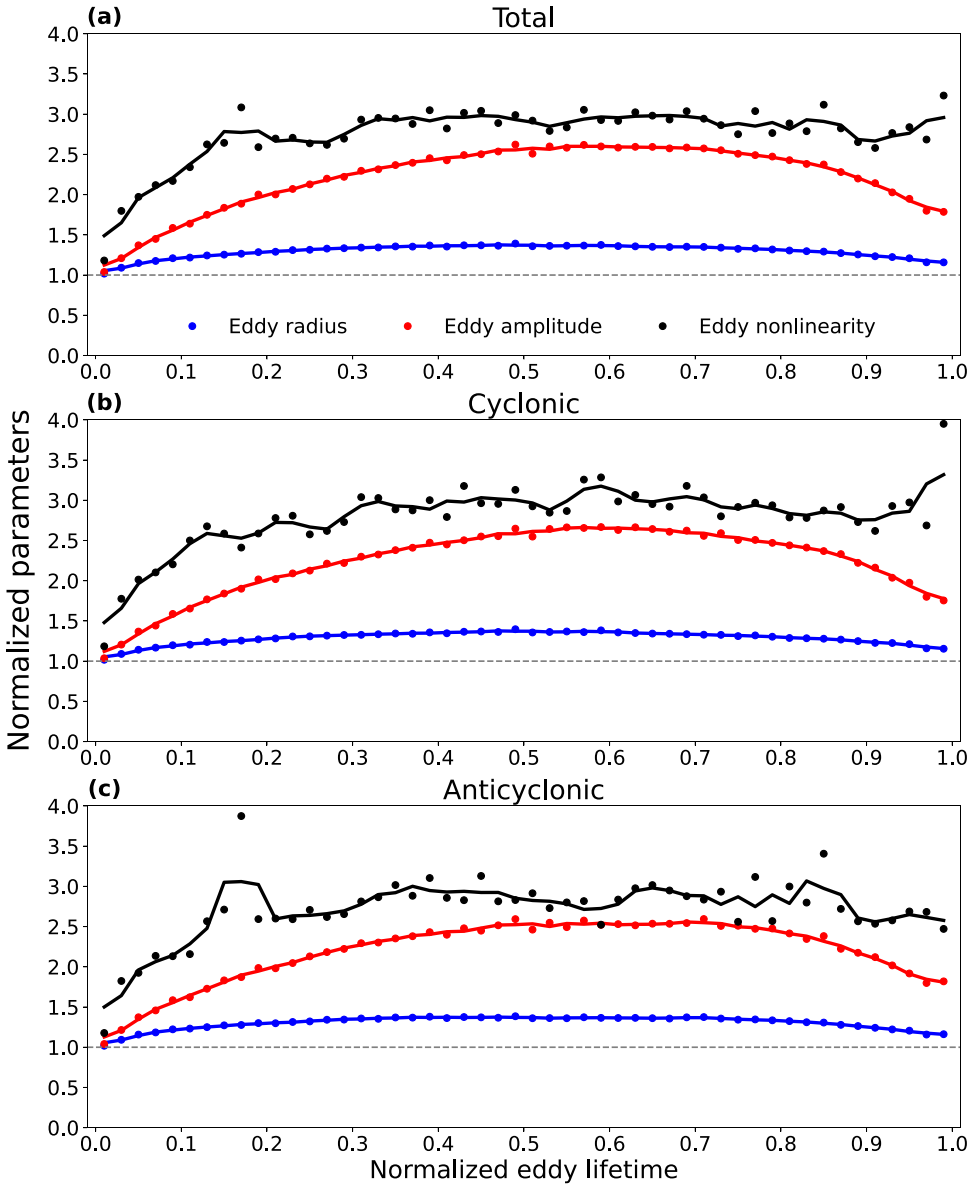

Fig. 4 Mean properties of eddies normalized by their lifetime and scaled by their initial value. Blue line corresponds to amplitude, red line corresponds to radius, and black line for eddy nonlinearity: (**a**) for the total number of eddies; (**b**) for CE and (**c**) for AE. Solid lines represent a 3-point moving average, except in the extremes (2-point moving average)

4.2 Spatial distribution of Caribbean Sea eddies

The total number of eddy observations (summed up in squares of 0.5°× 0.5°) are displayed in Fig. 5, left panel. At the northern basin, eddies are distributed in the whole domain with a larger number of observations at the edges constrained by the 500 m isobath, and the two branches flowing northwards, towards the Yucatan channel, and southwards, forming the Caribbean counter current (CCC) near Panama. Jouanno et al. (2008) already described permanent features involved in the formation/dissipation of eddies consisting of an anticyclonic recirculation of water in the south of Cuba and a cyclonic gyre, known as the Panama-Colombia gyre, characterized by the episodic formation of a CE that quickly dissipates when interacting with the southern Caribbean anticyclones.

Above features are illustrated by the Mean Eddy Kinetic Energy (MEKE), defined as MEKE $= u_g'^2 + v_g'^2$, where the prime stand for the time-dependent fluctuating part (the eddy component of the flow), averaged over 1993–2019, which is shown in Fig. 5, right. As expected, high values of MEKE correspond to the locations where the largest number of eddies are found (Fig. 5, left panel). MEKE has been computed with daily geostrophic velocities over the basin and its primary source of generation is the mean current instability, which acts in two ways to generate eddies; first, strong horizontally sheared motions result in barotropic instabilities where the energy source for generating eddies is the MKE, and secondly, the presence of a vertical shear in strong ocean fronts results in baroclinic instabilities where the energy required for eddy generation comes from the available potential energy due to isopycnal tilting. Both formation processes lead to hot spots of eddy energy.

Winds in the Caribbean are mainly driven by the location of the ITCZ and by the American Monsoon System, and present two climatic seasons: the dry season from December to March, and the wet season from August to November. During the dry season, northern easterlies dominate the area due to the location of the ITCZ at a latitude between 0°N and 5°N. During the wet season southern easterlies are able to reach the Colombian basin due to the migration of ITCZ towards higher latitudes (between 10°N and 12°N) (Orejarena-Rondón et al. 2019). Averaged wind streamlines for dry and wet seasons are depicted in Fig. 6, left and right panels respectively (see for completeness Fig. 11 in Appendix A for the monthly mean wind patterns over the Caribbean Sea). The spatial distribution of eddy observations during these two seasons (shading in both panels) shows a shift in the southern area of the basins between Panama and Colombia with more eddies approaching the continent. This is probably the result of the intensification of the Caribbean Countercurrent (CCC) induced by the shift of the ITCZ, which advects eastwards those eddies formed by the instability of the CC in the central basin.

It is worth to note that the highest density of eddy observations at the lee of the lesser Antilles is found at the left side of the SOM lattice that will be presented later (Fig. 9), and that they mostly represent the situation given in December–March (Fig. 10) which is the result of the interaction between the inflow of subtropical Atlantic waters of the NBC and the latitudinal wind displacement, which slightly shifts towards the southwest at the eastern boundary.

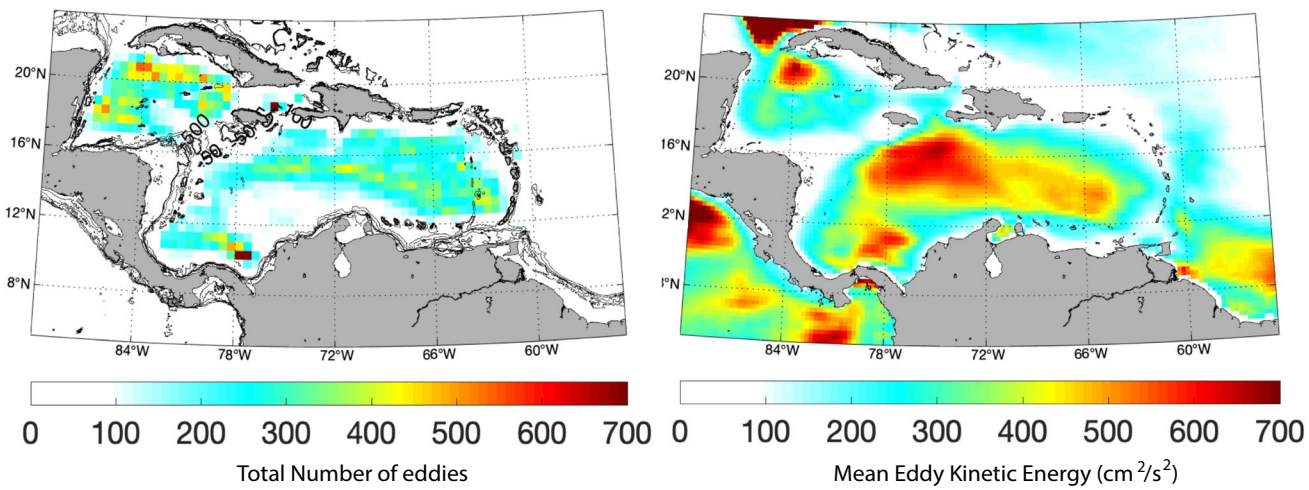

Fig. 5 Left: Total number of eddy observations from 1993 to 2019 within boxes of 0.5°× 0.5° side length. Isolines depict the 50, 100, 200, 500 and 1000 m isobaths. Right: MEKE derived from SSH geostrophic velocities for the period of 1993 to 2019. Units in cm^2/s^2

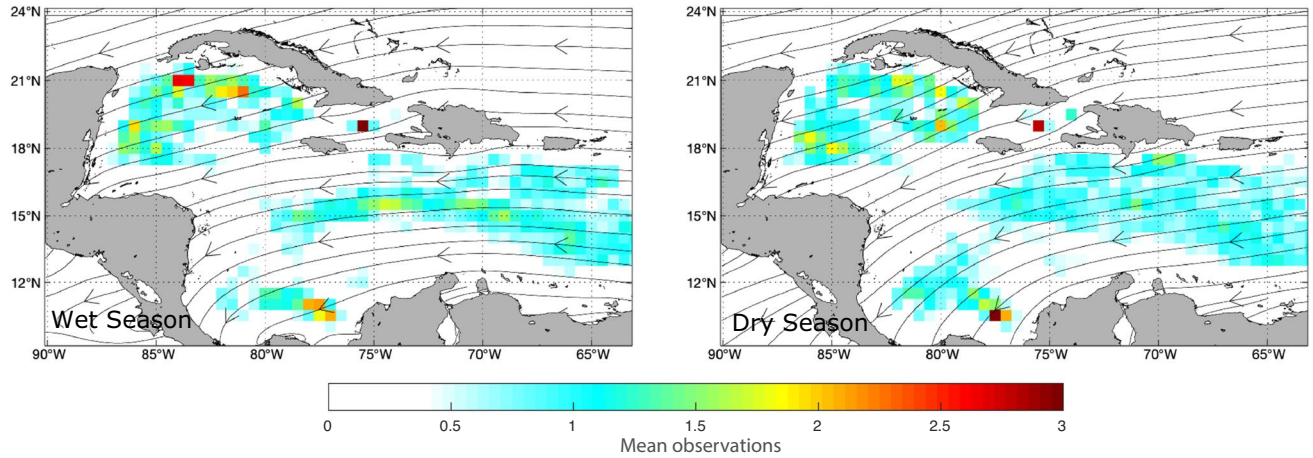

Fig. 6 Left: streamlines of 10 m height above sea level mean wind during the wet season (December–March), and average number of eddy observations detected for the same period. Right: the same as in the left but for the dry season (August–November). Wind product is the Cross-Calibrated Multi-Platform (CCMP) Version 2.0, which provides 6-hourly maps at a spatial resolution of 0.25°×0.25°. Data is available from 1988 and freely downloadable at http://www.remss.com/measurements/ccmp/

4.3 Monthly and seasonal variability of eddy observations

From the monthly distribution of eddy observations (summed in 0.5°× 0.5° bins), we perform a temporal analysis with the Kohonen Self-Organizing Maps (SOM). SOM is an unsupervised learning neural network especially suited to extract patterns from large data sets by means of a reduction of the high-dimensional feature space of the input data to a lower-dimensional network of units called neurons (Liu and Weisberg 2005; Hernández-Carrasco et al. 2018). In this study, we apply SOM to both space and time domains. In the spatial analysis, each neuron corresponds to a characteristic spatial pattern, showing a specific spatial distribution of the different values of eddy density. By identifying which of the extracted SOM spatial patterns is the most similar to the eddy density distribution for each date of the input time series (i.e., best matching unit, BMU), we can obtain the evolution over time of the characteristic spatial patterns. In the time domain analysis neurons show temporal patterns, and in this case we use the BMU to localize in the space each temporal pattern, providing a map of regions with different eddy density time variability.

By applying the SOM in the temporal domain, we can extract zones of covariability (i.e., those regions with a very similar temporal behavior). Each neuron is represented by a weighted vector with a number of components equal to the dimension of the input sample data. In each iteration the neuron whose weighted vector is more similar to the presented input sample data vector is updated together with its topological neighbors. At the end of the training process, the probability density function of the input data is approximated by the SOM, and each unit is associated with a reference pattern that has a number of components equal to the number of variables in the data set.

First, we compute the SOMs of the monthly eddy observations in the temporal domain with a map size of 3 × 2 (6 neurons or patterns) and a hexagonal map lattice. Figure 7 shows the six zones of eddy covariability in the Caribbean Sea (to be compared with Fig. 5, left) and Fig. 8 the temporal evolution of each of these zones. Each color corresponds to a zone with the same statistical behavior regarding the number of eddy observations.

The largest area (77% of the total coverage) corresponds to pattern P6 (orange color) where eddy observations are roughly detected (Fig. 9). This area covers the northeastern side of the domain (within the Atlantic basin) and Caribbean Sea shelf areas, far from the main currents and their instabilities induced by the latitudinal ITCZ migration, and also near the coast where SLA presents the largest uncertainties. The second largest percentage (13% of coverage) is given by P1 which, as already has been pointed out, follows the spatial distribution of MEKE. The monthly number of eddy observations in this area is on average 0.7 (Fig. 8, top right panel). The averaged monthly detected eddy observations (box inside Fig. 7) does not display large differences in the detected observations throughout the year. The rest of the patterns (from P2 to P5) cover between 5.5% and 1% of the area, with mean monthly detected eddy observations ranging between 0.1 (P3) and 0.3 (P4).

Next, the monthly distribution of eddy observations is analyzed together with the MEKE derived from SSH-based geostrophic velocities. We follow the same procedure explained above, but in this case we are interested in obtaining the spatial distribution of both fields (Hernández-Carrasco and Orfila 2018). Hence, we are going to apply the SOM in the spatial domain (Fig. 9 shows the 6 neurons for the monthly eddy observations distribution and their

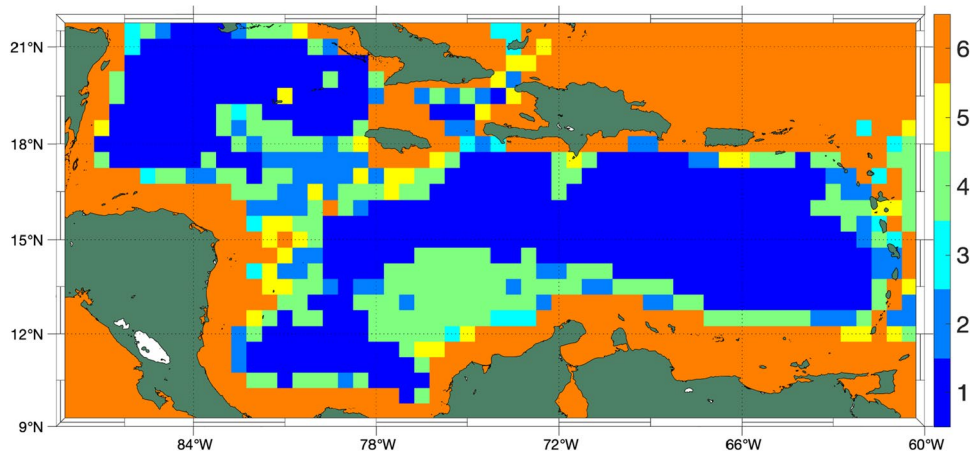

Fig. 7 Zones of covariability in a 3 × 2 SOM lattice for the monthly distribution of eddy observations between 1993 and 2019. Each color corresponds to a neuron

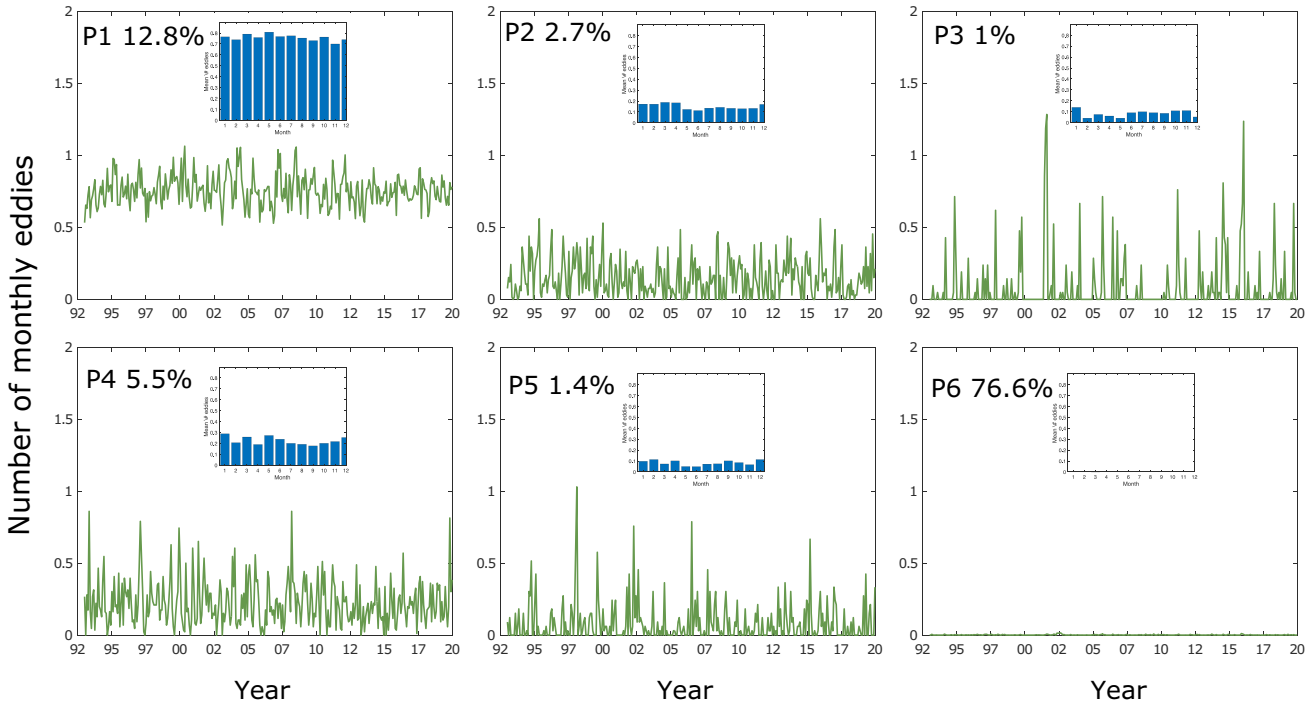

Fig. 8 Temporal evolution of eddy observations patterns detected inside each of the 6 areas shown in Fig. 7. The probability of occurrence of each pattern is indicated within each panel. Inner figures correspond to the monthly distribution of eddy observations associated to each amplitude

corresponding MEKE). The probability of occurrence of the each pattern is included at the top right of the upper six panels. The most repeated patterns are P3 and P4. The former shows a similar MEKE distribution with the only major difference observed at the CCC, which extends towards the Colombian coast. Although small differences are apparent in P3, eddies are more southerly distributed occupying the whole central American shore, thus being further advected westwards. Looking at the MEKE associated to P3 and P4, they clearly represent the wet season (P3) and the dry season (P4), respectively, when wind stress is larger at the southern basin inducing high values of MEKE thus rising on average the number of eddies in this area during this season.

To further study the temporal distribution of patterns we have computed the monthly probability of occurrence of spatial patterns from the BMUs (Fig. 10). The wet season is mainly represented by P3, while P4 dominates during the dry season, being in the latter when eddies can reach the southern side of the basin, thus transporting water from the central basin towards the more coastal Caribbean areas.

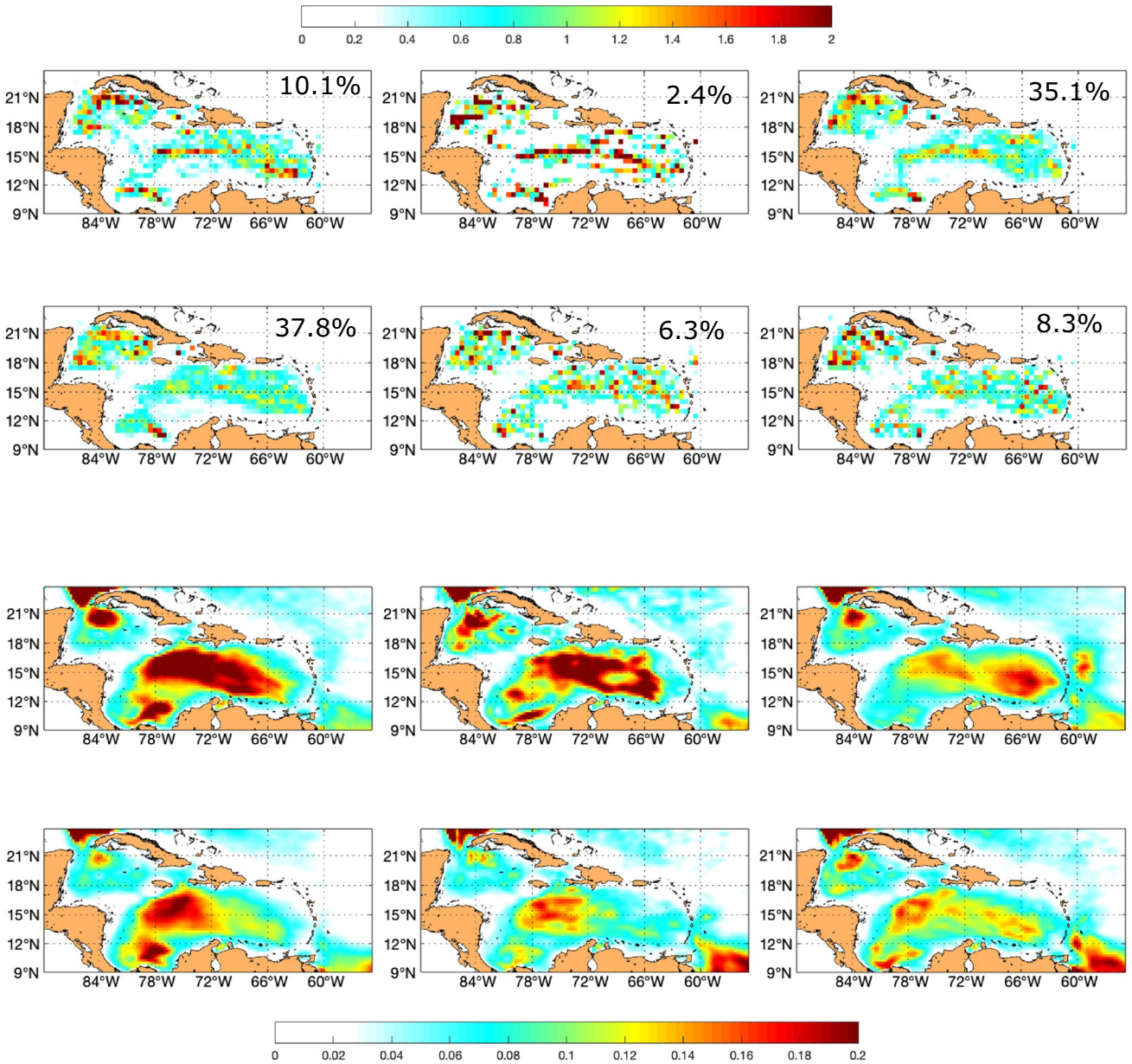

Fig. 9 SOM neurons in a 3 × 2 lattice for the monthly distribution of eddy observations (top panels), and their associated $(MEKE)^{1/2}$ patterns (bottom panels). Units in m/s

During the windy season, strong southwestwards winds with their maximum located in the center of the basin produce a strong cross-shore Ekman transport towards the north-northwest, thus contributing to increase MEKE in central Caribbean Sea regions. During these windy months, eddy observations are mainly distributed over the CC, with a larger distribution over the northern basin. By contrast, during mild wind periods (e.g., October), the most representative pattern is P2, in which both the CC and the CCC are well developed (see Fig. 9 and Fig. 10), as discussed in Orfila et al. (2021).

5 Conclusions

The work here presented has described the main statistical characteristics as well as the seasonal variability of mesoscale eddies derived from SLA in the Caribbean Sea between 1993 and 2019. A better understanding of the variability of eddies and their spatial distribution provides new knowledge on their mechanisms of formation, intensification and dissipation, which have strong implications on biogeochemical and air-sea exchange processes. Since the Caribbean Sea is a semi-enclosed basin, a large part of the

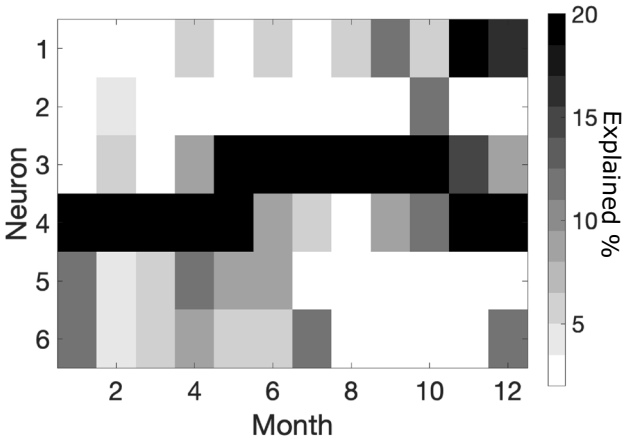

Fig. 10 Monthly distribution of the patterns provided in Fig. 9

advection of nutrients and heat, both in the vertical and in the horizontal, are due largely to eddies.

The spatial distribution of mesoscale eddies reported in this work is consistent with findings from previous observational and model-based studies in which most of the eddies were found to be formed in the eastern Caribbean Sea, or alternatively, had already formed in the northeast of Brazil, although we have also detected a significant number of eddies born in the Yucatan basin. Some of them stay some time off the Colombian and Venezuelan coasts, while the reminder tend to redistribute around the Cayman and Yucatan basins (Carton and Chao 1999; Andrade and Barton 2000; Oey and Lee 2003; Jouanno et al. 2008; Richardson 2005; Jouanno et al. 2009; Chelton et al. 2011).

Although many works (Carton and Chao 1999; Oey and Lee 2003; Richardson 2005; Jouanno et al. 2008; van der Boog et al. 2019) have presented a preference for anticyclonic polarity in the Caribbean sea, in this work we find a larger number of CE (54%) than ACE (46%). There are not significant differences in their respective origin, propagation, amplitude, radius or nonlinearity, although on average CE tend to be more nonlinear than ACE, while ACE are slightly larger. The latter result is in agreement with Jouanno et al. (2008), who found that the largest eddies in the Caribbean Sea are anticyclones. The mean lifetime of detected eddies is about two months, although they vary between a few weeks and about 10 months. Most eddies travel westwards, although a few move eastwards. Most eddies (> 85%) have a lifetime shorter than 120 days. Comparing the results from Carton and Chao (1999) and Oey and Lee (2003), who found the period of spin-up, growth, and drift is approximately 100 days, and with those from Andrade and Barton (2000), who found that the typical timescale of synoptic eddies traveling through the Caribbean Sea is between 100 and 130 days, it can be concluded that there are no differences between polarities and that there is a general agreement with their longevity.

The mean radius detected, 100 ± 31 km for CE (Fig. 3h) and 108 ± 32 km for AE (Fig. 3i) does not agree with the one provided by Jouanno et al. (2008), although our results are consistent with the latitudinal distribution of eddy sizes described by Chelton et al. (2011), in which eddies of around 100 km of radius are found in the near-equatorial regions to monotonically decrease up to 80 km at 20° of latitude. On the other hand, the mean value of the amplitude (7 ± 4 cm for CE and 7 ± 4 cm for AE, see Fig. 3e and f, respectively), is consistent with Gaube (2013), who found that the eddy field in the Caribbean Sea is characterized by mesoscale eddies with average amplitudes of 7.8 cm. We found that eddies are strongly nonlinear, especially CE, with a mean value close to 4.

Eddies mostly dissipate near the coast of Nicaragua or the Yucatan peninsula, and only a few of them are able to travel northwards crossing the Yucatan basin as already noted by Carton and Chao (1999) and Chelton et al. (2011), who pointed out that eddy disappearance is more frequent near the western boundaries. However, eddy dissipation in the open ocean can occur by frictional decay or coalescence with other eddies as a consequence of the up-scale energy cascade of geostrophic turbulence. Some of these terminations may also occur from temporary or permanent loss of an eddy by the tracking procedure because of noise in the SLA field or imperfections of the tracking algorithm (Chelton et al. 2011). In this regard, Amores et al. (2018) also noted that the number of detected eddies can be significantly underestimated due to the interpolation and filtering methods behind the construction of gridded SLA fields, which could be removing some real SLA eddy-like anomalies. Besides, the transfer of vorticity from the atmosphere to the ocean and the seasonal variability in the atmospheric forcing may play an important role in the dissipation of eddies in the basin. Only few detected eddies are able to pass through the Chibcha Channel towards the Cayman Sea. Eddies which originated in the southwestern Caribbean Basin are the only ones not advected by the Caribbean Current nor affected by its instabilities. These eddies tend to remain in the southwestern Caribbean Sea where they form distinctive SLA patterns. Richardson (2005) pointed out that many anticyclonic eddies travel westwards up to the Jamaica Ridge when they are disrupted by topographic-induced dissipation.

A seasonal classification of the spatial distribution of eddy observations through a neural network based on Self Organized Maps (SOM) showed that the most representative patterns differ when the analysis is performed by seasons. The most representative patterns are P4 for the dry season and P3 for the wet season (Fig. 9). In both cases eddy observations tend to accumulate in the interior of the basin and off the western Colombian basin, where eddies probably tend to stay longer time due to a partial topographic constraint. However, the complex spatial distribution of eddies has a periodicity that needs to be further analyzed in future research.

An open question for a follow-up study is how these mesoscale structures are linked to large scale climate variability, such as El Niño-Southern Oscillation (e.g., Sayol et al. 2022), or other signals like the North Atlantic Oscillation or the Pacific Decadal Oscillation.

Appendix A Monthly mean surface wind over the Caribbean Sea

Cross-Calibrated Multi-Platform (CCMP) near-surface horizontal quasi-global wind fields (u, v)—at 10 m over the sea level—have been used in its version 2.0. Winds are provided since 1987 with a spatial resolution of $0.25^{\circ} \times 0.25^{\circ}$ every 6 hours and covers almost all Earth (except poles). This product is the result of an optimal merging of different radiometers, scatterometers, buoys and model data using a variational analysis method.

The monthly mean wind is shown in Fig. 11. Wind streamlines depict the westward direction of the Caribbean low level jet. The maximum wind intensity is presented during February and July, while the minimum occurs during May and October. For a more detailed explanation on the Caribbean Low level jet and its role on the circulation and dynamics of the region the reader is referred to Orfila et al. (2021) and articles therein.

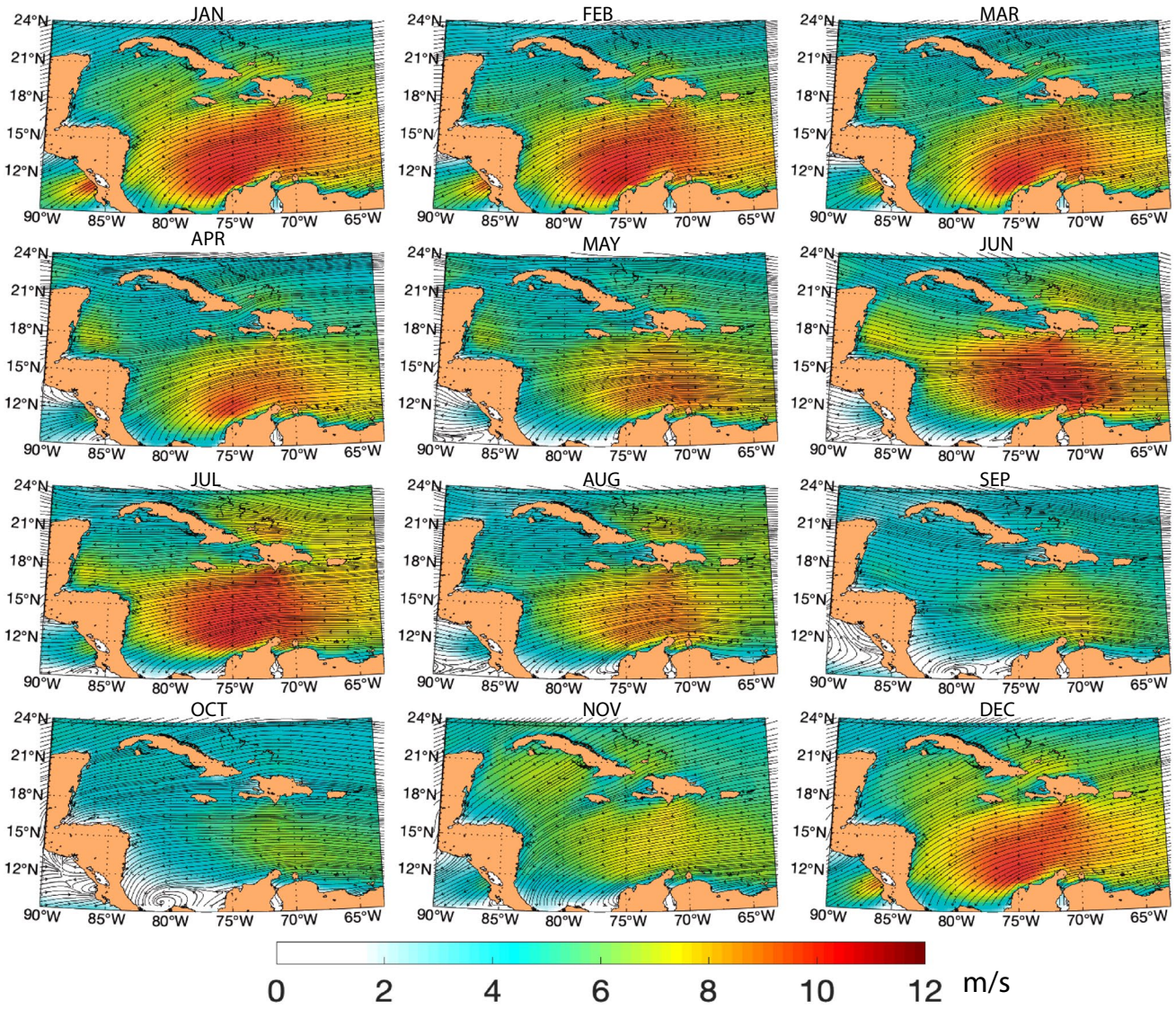

Fig. 11 Monthly wind intensity and streamlines in the Caribbean sea

Appendix B Eddy identification

In the following we describe the process followed to identify eddies contained in the eddy atlas (AVISO 2020):

(i) For each time, there is a two-dimensional value of SSH, $h(i,j)$, with four neighbors. For anticyclonic eddies—concave downward SSH—the identification is made by defining a pixel (i_{ext},j_{ext}) as a local positive extreme if the SSH values of its four neighbors are less than or equal to $h(i_{ext},j_{ext})$. Likewise, for cyclonic eddies—concave upward SSH—a pixel (i_{ext},j_{ext}) is defined to be a local negative extreme if the SSH values of its four neighbors are greater than or equal to $h(i_{ext},j_{ext})$.

(ii) If we assume an anticyclonic eddy with a local maximum SSH at grid location (i_{ext},j_{ext}) and an indicated threshold SSH value $h_t \leq h(i_{ext},j_{ext})$, it is possible to define $E(i_{ext},j_{ext},h_t)$ as the connected set of pixels (i_l,j_l), $l=1,..,n$, which contains (i_{ext},j_{ext}) and satisfies $h(i_l,j_l) \geq h_t$, $l=1,...,n$. Later, some criteria is applied to seek h_b, the minimum value of incrementally decreasing thresholds h_t, such that the compact and coherent structure $E(i_{ext},j_{ext},h_b)$, which is an eddy realization with basic SSH value of h_b, satisfies:

  (a) $n \leq n_{max}$, a determined number of pixels in this structure.
  (b) $n \geq 2$, a minimum of two interior pixels.
  (c) Not a single pixel in this structure could have as a neighbor a pixel that belongs to another eddy.
  (d) The structure is connected. There are not holes on the edges or within the interior of the area.
  (e) Let $d(i_k,j_k,i_l,j_l)$ be the distance between pixels (i_k,j_k) and (i_l,j_l). So, the maximum value of $d(i_k,j_k,i_l,j_l)$ over all pairs of edge pixels in the structure $E(i_{ext},j_{ext},h_t)$ must be less than a specified value d_{max}.

(iii) The set of edge pixels in $E(i_{ext},j_{ext},h_b)$ defines the outer perimeter of the eddy realization.

(iv) Eddies are identified by growing sets of pixels from the single pixels at the local maximum in $h(i,j)$ and $-h(i,j)$ for anticyclonic and cyclonic eddies, respectively. Hence, given a set of pixels E_l, the next set E_{l+1} is computed by finding all of the neighbors of the edge pixels in E_l that exceed h_{l+1}, which are then added to E_l. At each step E_l, all the criteria above described are checked. If at least one of them is missing, the sequence is stopped. The single pixels at the local maximum are ordered into decreasing size and eddy recognition are obtained from successively smaller initial values of h or $-h$ without attention to polarity.

After we identify the eddies we calculate the different eddy characteristics using the following parameters:

1. The eddy centroid coordinates—longitude and latitude (x_c,y_c).
2. The amplitude A defined as the difference between the extreme SSH value of $h(i_{ext},j_{ext})$ and the average of SSH over the edge pixels that define the external perimeter of the eddy.
3. The effective radius scale L_{eff}, which is defined to be the radius of a circle with area equal to that of the set of connected pixels $E(i_{ext},j_{ext},h_b)$.
4. The average of geostrophic speed covering the edge pixels of E_l is found at each threshold $h_l \geq h_n$. The maximum of this average is the rotational or axial speed U of the eddy where, h_U is defined as the threshold SSH at which this maximum average occurs. The speed core of the eddy is then the subset of connected pixels $E(i_{ext},j_{ext},h_U)$.
5. The speed-based radius scale L, which is defined to be the radius of a circle which area is equal to that enclosed by the contour of maximum circum-average geostrophic speed.

This algorithm is applied on a $1/4^{\circ} \times 1/4^{\circ}$ grid using a threshold increment of $\delta = 0.25$ cm and a maximum area $n_{max} = 2000$ pixels. The distance d between the two remotest points must be less than $d_{max} = 400km$ for latitudes greater than $\pm 25^{\circ}$ and $d_{max} = 700$ km lower than $\pm 25^{\circ}$ of latitude at the equator, plus an additional restriction of eddies amplitude $A \geq 1$ cm (Schlax and Chelton 2016).

Acknowledgements The authors would like to thank comments from two anonymous referees.

Author Contributions M.E. López-ALzate (MELA) developed the statistics, J.M. Sayol (JMS) developed the seasonal analysis and A.Orfila (AO) performed the spatio-temporal variability. AO and JMS produced and analyzed the results with the support of MELA. All authors have read, reviewed and approved the submitted version of the manuscript.

Funding Open Access funding provided thanks to the CRUE-CSIC agreement with Springer Nature. JMS received the joint funding from the Generalitat Valenciana and the European Social Fund under Grant APOSTD/2020/254. AO received financial support from projects Mocca and Lamarca (grants # RTI2018-093941-B-C31 and PID2021-123352OB-C31) funded by MCIN/AEI/ and by "ERDF A way of making Europe", and from Fundación Iberostar and Université de Toulon-VAR. MELA is funded by Corporación CE-Marin through Convocatoria 14, 2018 supporting PhD candidates.

Data Availability All codes are available from the corresponding author upon request. Mesoscale eddy atlas is available from AVISO at https://www.aviso.altimetry.fr/en/data/products/value-added-products/global-mesoscale-eddy-trajectory-product.html (last access 25/05/2021). Geostrophic velocities provided by CMEMS are available at https://climate.copernicus.eu (last access 5/01/2022). Winds are available from

RMSS at http://www.remss.com/measurements/ccmp/ (last access 25/02/2022).

Declarations

Ethics approval Not applicable

Consent for publication Not applicable

Consent to participate Not applicable

Competing interests The authors declare that they have no known competing financial interests or personal relationships that could have appeared to influence the work reported in this paper. AO is member of the editorial board of Ocean Dynamics, Ocean Science and Frontiers in Marine Science.

References

Amores A, Jorda G, Arsouze T et al (2018) Up to what extent can we characterize ocean eddies using present-day gridded altimetric products? J Geophys Res: Oceans 123(10):7220–7236. https://doi.org/10.1029/2018JC014140

Andrade CA (2000) The circulation and variability of the colombian basin in the caribbean sea. PhD thesis, University of Wales

Andrade CA, Barton ED (2000) Eddy development and motion in the caribbean sea. J Geophys Res 105(C11):26,191-26,201. https://doi.org/10.1029/2000JC000300

Andrade CA, Barton ED (2005) The guajira upwelling system. Cont Shelf Res 25(9):1003–1022. https://doi.org/10.1016/j.csr.2004.12.012

AVISO (2020) Mesoscale Eddy Trajectory Atlas Product Handbook

Baums IB, Paris CB, Chérubin LM (2006) A bio-oceanographic filter to larval dispersal in a reef-building coral. Limnol Oceanogr 51(5):1969–1981. https://doi.org/10.4319/lo.2006.51.5.1969

van der Boog CG, Pietrzak JD, Dijkstra HA et al (2019) The impact of upwelling on the intensification of anticyclonic ocean eddies in the caribbean sea. Ocean Sci 15(6):1419–1437. https://doi.org/10.5194/os-15-1419-2019

Bracco A, Pedlosky J, Pickart RS (2008) Eddy formation near the west coast of greenland. J Phys Oceanogr 38(9):1992–2002. https://doi.org/10.1175/2008JPO3669.1

Capet X, McWilliams JC, Molemaker MJ et al (2008) Mesoscale to submesoscale transition in the california current system. Part I: flow structure, eddy flux, and observational tests. J Phys Oceanogr 38(1):29–43. https://doi.org/10.1175/2007JPO3671.1

Carton JA, Chao Y (1999) Caribbean sea eddies inferred from topex/poseidon altimetry and a 1/6° atlantic ocean model simulation. J Geophys Res 104. https://doi.org/10.1029/1998JC900081

Chang YLK, Miyazawa Y, Béguer-Pon M et al (2018) Physical and biological roles of mesoscale eddies in japanese eel larvae dispersal in the western north pacific ocean. Sci Rep 8(1):5013–5013. https://doi.org/10.1038/s41598-018-23392-5

Chelton DB, de Szoeke RA, Schlax MG, El Naggar K, Siwertz N (1998) Geographical variability of the first baroclinic rossby radius of deformation. J Phys Oceanogr 28(3):433–460. https://doi.org/10.1175/1520-0485(1998)028⟨0433:GVOTFB⟩2.0.CO;2

Chelton DB, Schlax MG, Samelson RM (2011) Global observations of nonlinear mesoscale eddies. Prog Oceanogr 91(2):167–216. https://doi.org/10.1016/j.pocean.2011.01.002

Chérubin LM, Richardson P (2007) Caribbean current variability and the influence of the amazon and orinoco freshwater plumes. Deep-Sea Res I Oceanogr Res Pap 54:1451–1473. https://doi.org/10.1016/j.dsr.2007.04.021

Conti D, Orfila A, Mason E et al (2016) An eddy tracking algorithm based on dynamical systems theory. Ocean Dyn 66(11):1415–1427. https://doi.org/10.1007/s10236-016-0990-7

Farneti R, Delworth TL, Rosati AJ et al (2010) The role of mesoscale eddies in the rectification of the southern ocean response to climate change. J Phys Oceanogr 40(7):1539–1557. https://doi.org/10.1175/2010JPO4353.1

Fratantoni DM, Richardson PL (2006) The evolution and demise of north Brazil current rings*. J Phys Oceanogr 36(7):1241–1264. https://doi.org/10.1175/JPO2907.1

Gaube P (2013) Satellite observations of the influence of mesoscale ocean eddies on near-surface temperature phytoplankton and surface stress. PhD thesis, Oregon State University

Gaube P, Chelton D, Samelson RM et al (2015) Satellite observations of mesoscale eddy-induced ekman pumping. J Phys Oceanogr 45(45,1):104–132. https://doi.org/10.1175/JPO-D-14-0032.1

Goni GJ, Johns WE (2003) Synoptic study of warm rings in the north Brazil current retroflection region using satellite altimetry. In: Goni G, Malanotte-Rizzoli P (eds) Interhemispheric water exchange in the atlantic ocean, elsevier oceanography series. https://doi.org/10.1016/S0422-9894(03)80153-8, vol 68. Elsevier, pp 335–356

Hernández-Carrasco I, Solabarrieta L, Rubio A et al (2018) Impact of hf radar current gap-filling methodologies on the lagrangian assessment of coastal dynamics. Ocean Sci 14(4):827–847. https://doi.org/10.5194/os-14-827-2018

Hernández-Carrasco I, Orfila A (2018) The role of an intense front on the connectivity of the western mediterranean sea: the cartagena-tenes front. J Geophys Res: Oceans 123(6):4398–4422. https://doi.org/10.1029/2017JC013613

Ji J, Dong C, Zhang B et al (2018) Oceanic eddy characteristics and generation mechanisms in the kuroshio extension region. J Geophys Res: Oceans 123(11):8548–8567. https://doi.org/10.1029/2018JC014196

Jochumsen K, Rhein M, Böning SHCW (2010) On the propagation and decay of north Brazil current rings. J Geophys Res 115. https://doi.org/10.1029/2009jc006042

Johns WE, Townsend TL, Fratantoni DM et al (2002) On the atlantic inflow to the caribbean sea. Deep-Sea Res I(49):211–243. https://doi.org/10.1016/S0967-0637(01)00041-3

de Jong MF, Bower AS, Furey HH (2016) Seasonal and interannual variations of irminger ring formation and Boundary–Interior heat exchange in FLAME. J Phys Oceanogr 46(6):1717–1734. https://doi.org/10.1175/JPO-D-15-0124.1

Jouanno J, Sheinbaum J, Barnier B et al (2008) The mesoscale variability in the caribbean sea. part i: Simulations and

characteristics with an embedded model. Ocean Model 23:82–101. https://doi.org/10.1016/j.ocemod.2008.04.002
Jouanno J, Sheinbaum J, Barnier B et al (2009) The mesoscale variability in the caribbean sea. part ii: Energy sources. Ocean Model 26:226–239. https://doi.org/10.1016/j.ocemod.2008.10.006
Jury MR (2011) Long-term variability and trends in the caribbean sea. International Journal of Oceanography 2011. https://doi.org/10.1155/2011/465810
Karstensen J, Schütte F, Pietri A et al (2017) Upwelling and isolation in oxygen-depleted anticyclonic modewater eddies and implications for nitrate cycling. Biogeosciences 14(8):2167–2181. https://doi.org/10.5194/bg-14-2167-2017
Liu Y, Weisberg RH (2005) Patterns of ocean current variability on the west florida shelf using the self-organizing map. Journal of Geophysical Research: Oceans 110(C6). https://doi.org/10.1029/2004JC002786
Mason E, Pascual A, McWilliams JC (2014) A new sea surface Height–Based code for oceanic mesoscale eddy tracking. J Atmos Ocean Technol 31(5):1181–1188. https://doi.org/10.1175/JTECH-D-14-00019.1
Molinari R, Spillane M, Brooks I et al (1981) Surface current in the caribbean sea as deduced from lagrangian observations. J Geophys Res 86. https://doi.org/10.1029/JC086iC07p06537
Oey LY, Lee HC (2003) Effects of winds and caribbean eddies on the frequency of loop current eddy shedding: A numerical model study. Journal of Geophysics Research 108. https://doi.org/10.1029/2002JC001698
Orejarena-Rondón AF, Sayol JM, Marcos M et al (2019) Coastal impacts driven by sea-level rise in cartagena de indias. Frontiers in Marine Science 6. https://doi.org/10.3389/fmars.2019.00614
Orejarena-Rondón AF, Restrepo JC, Correa-Metrio A et al (2022) Wave energy flux in the caribbean sea: Trends and variability. Renew Energy 181:616–629. https://doi.org/10.1016/j.renene.2021.09.081
Orfila A, Urbano-Latorre CP, Sayol JM, et al. (2021) On the impact of the caribbean counter current in the guajira upwelling system. Frontiers in Marine Science 8. https://doi.org/10.3389/fmars.2021.626823
Pauluhn A, Chao Y (1999) Tracking eddies in the subtropical northwestern atlantic ocean. Phys Chem Earth Part A 24(4):415–421. https://doi.org/10.1016/S1464-1895(99)00052-6
Rennie SJ, Pattiaratchi CP, McCauley RD (2007) Eddy formation through the interaction between the leeuwin current, leeuwin undercurrent and topography. Deep Sea Res II: Top Stud Oceanogr 54(8):818–836.
Richardson PL (2005) Caribbean current and eddies as observed by surface drifters. Deep-Sea Res II(52):429–463. https://doi.org/10.1016/j.dsr2.2004.11.001
Sayol JM, Vásquez LM, Valencia JL et al (2022) Extension and application of an observation-based local climate index aimed to anticipate the impact of el niño–southern oscillation events on colombia. International Journal of Climatology n/a(n/a). https://doi.org/10.1002/joc.7540
Schlax MG, Chelton DB (2016) The "growing method" of eddy identification and tracking in two and three dimensions. College of Earth, Ocean and Atmospheric Sciences Oregon State University, Corvallis, Oregon
Schneider T, Bischoff T, Haug GH (2014) Migrations and dynamics of the intertropical convergence zone. Nature 513(7516):45–53. https://doi.org/10.1038/nature13636
Soutelino RG, Gangopadhyay A, da Silveira I (2013) The roles of vertical shear and topography on the eddy formation near the site of origin of the brazil current. Cont Shelf Res 70:46–60